Supporting Information

Self-assembly magnetized MXene avoid dual-agglomeration with enhanced interfaces for Strong Microwave Absorption through Tunable Electromagnetic Property

Xiao Li, Wenbin You, Lei Wang, Jiwei Liu, Zhengchen Wu, Ke Pei, Yuesheng Li, Renchao Che.*

Laboratory of Advanced Materials, Department of Materials Science and Collaborative Innovation Center of Chemistry for Energy Materials (iChem), Fudan University, Shanghai 200438, P. R. China

*E-mail: rcche@fudan.edu.cn

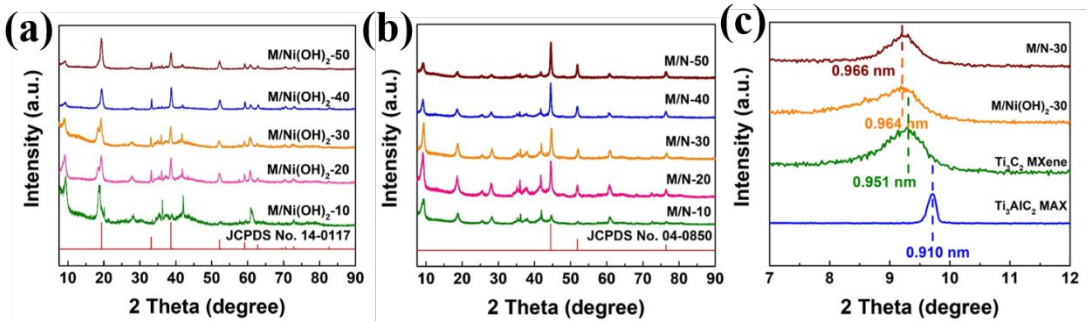

Figure S1. XRD patterns of as-prepared MXene/$Ni(OH)_2$ composites (a) and MXene/Ni composites (b), magnification of XRD patterns of MAX, MXene, MXene/$Ni(OH)_2$-30 and MXene/Ni-30 nanocomposites (c).

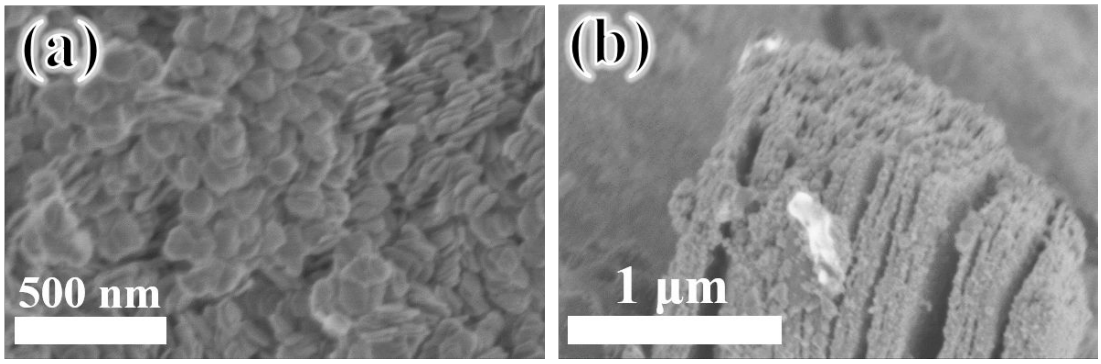

Figure S2. SEM images of $Ni(OH)_2$ (a) and M/N-30 (b).

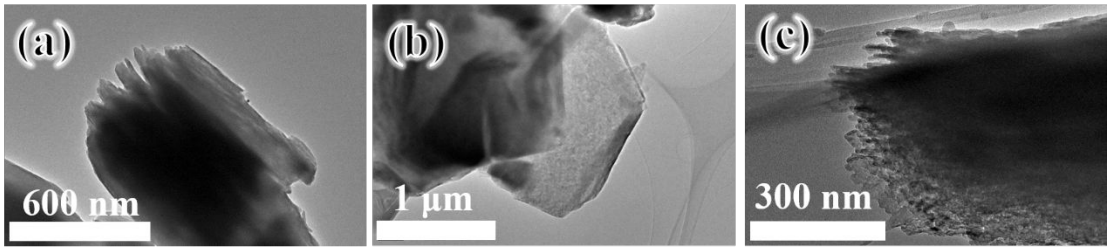

Figure S3. TEM images of MXene (a, b) and M/N-30 (c).

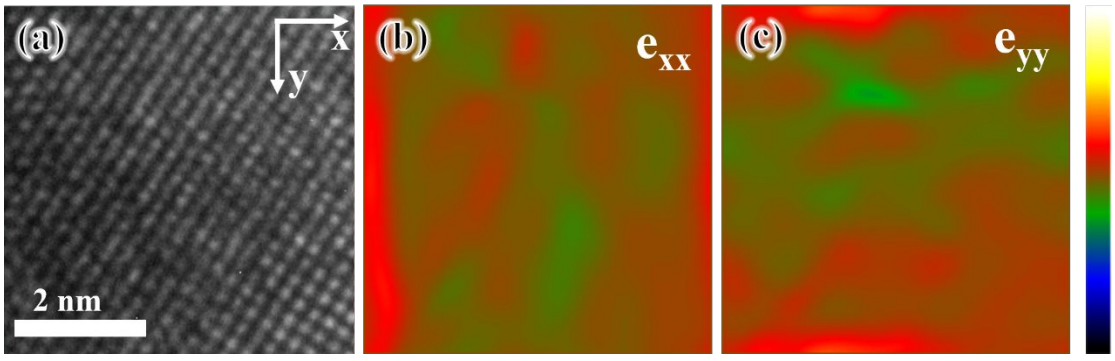

Figure S4. HRTEM images (a) and corresponding strain maps of the pure Ni (b, c). The color variation indicates the strain values ranging from -0.5 to 0.5.

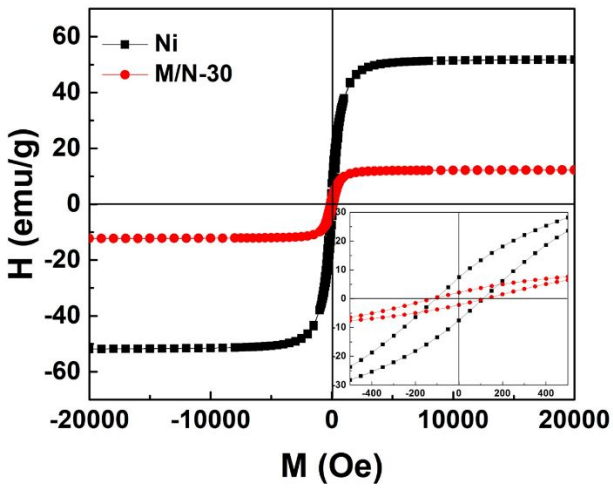

Figure S5. Hysteresis loops of Ni and M/N-40 measured at 300K. The inset gives an enlarged view of the hysteresis loops (-400 Oe – 400 Oe).

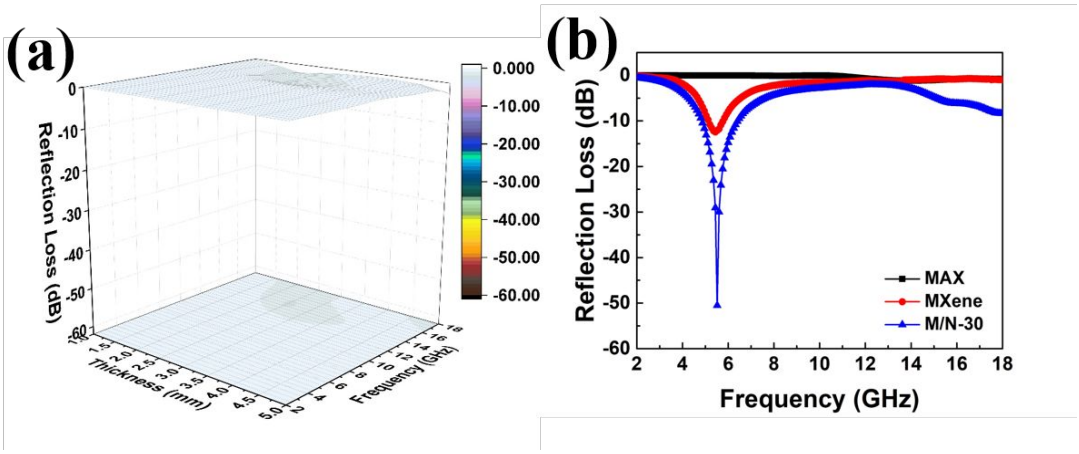

Figure S6. 3D representations of RL of MAX (a) and compared RL curves about MAX, MXene and M/N-30 samples with highest microwave absorption performance (b).

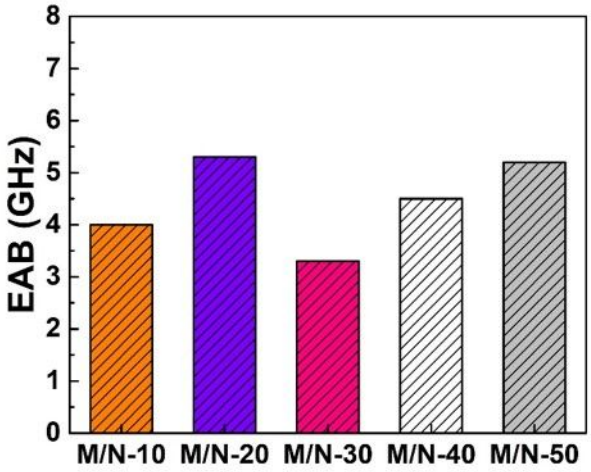

Figure S7. comparison of the maximum EAB of five different M/N composites.

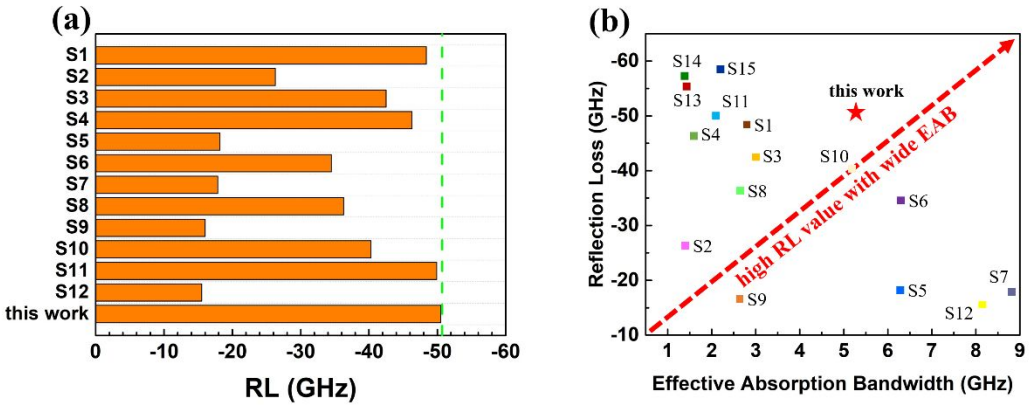

Figure S8. Comparison of MXene-based composites with minimum microwave absorption value (a); comparison of MXene-based composites with RL and EAB (b).

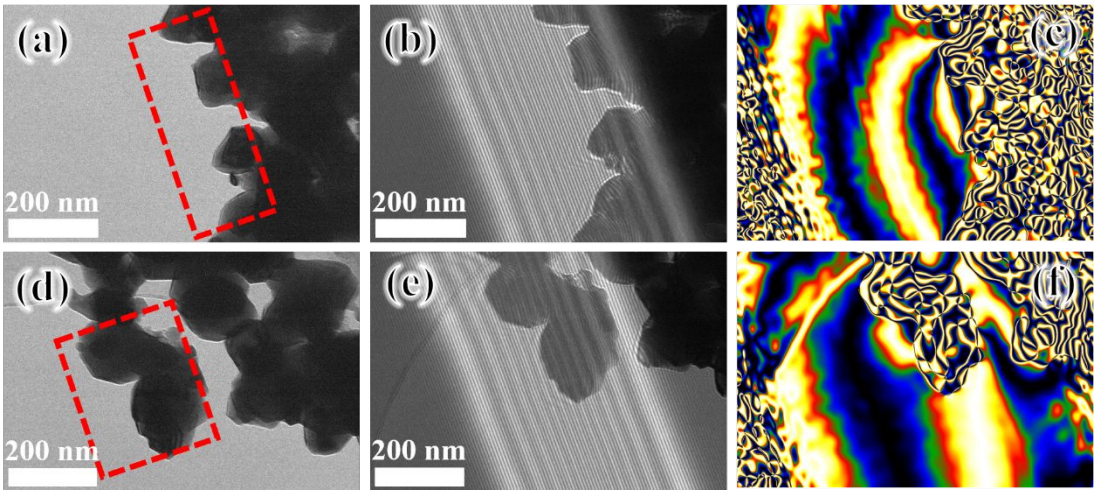

Figure S9. TEM image (a, d), off-axis electron holograms of cutting sections (b, e), off-axis electron holograms (c, f) of pure agglomerated Ni nanoparticles and the phase amplification of the holograms are 2.

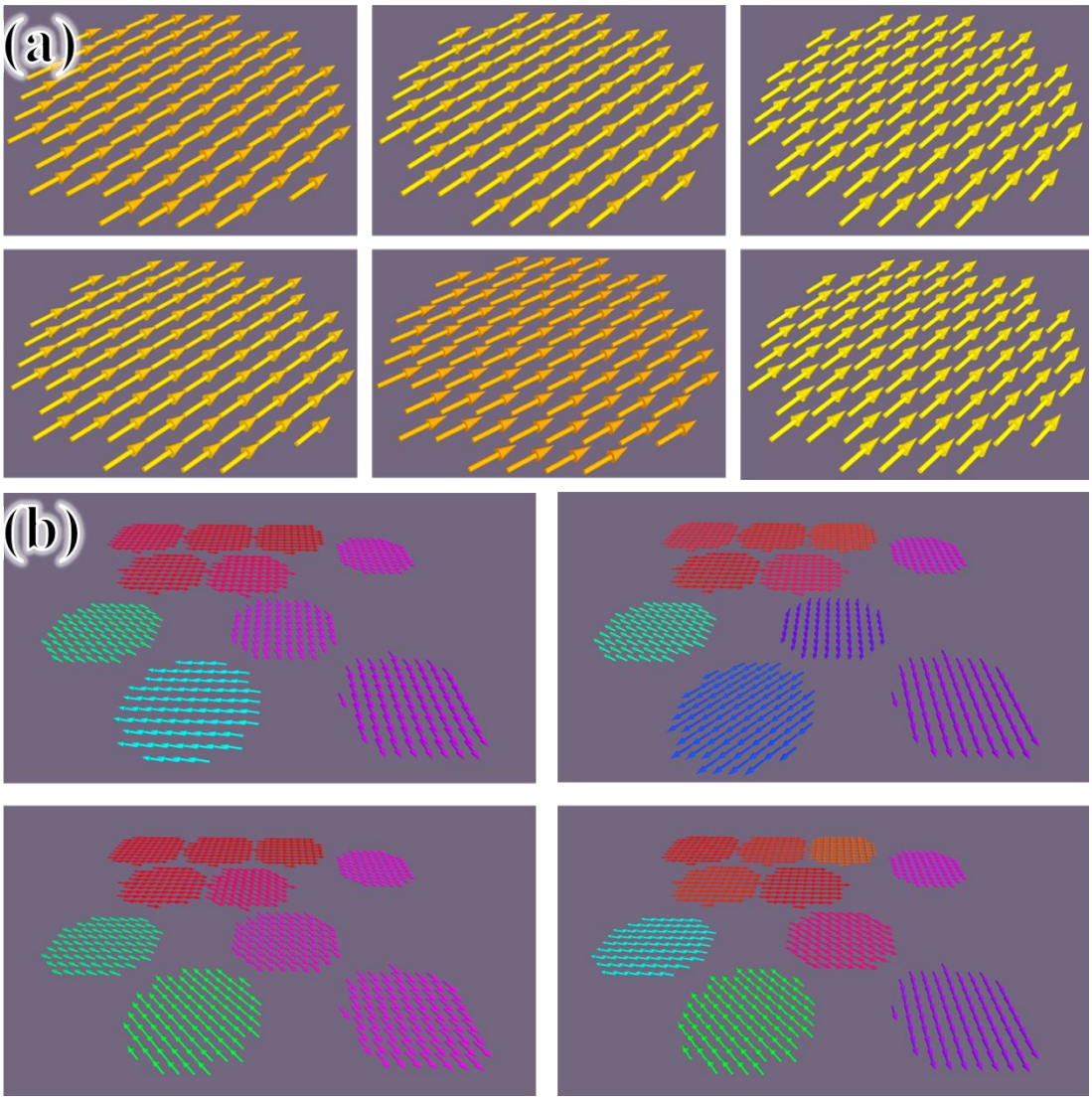

Figure S10. The cyclical variation of magnetic moments of the individual Ni nanoparticle (a) and numerous Ni nanoparticle (b) under an alternating magnetic field obtained from computational micromagnetic simulation. The size of circular Ni nanoparticle is 20*2 nm. The frequency of external magnetic field is 2 GHz.

Table S1. Comparison of microwave absorption performance among the reported MXene-based composites and the as-prepared MXenes/Ni.

Absorber	RL_{min} (dB)	Matching frequency (GHz)	EAB (GHz)	Thickness (mm)	refs
MXene/amorphous carbon/TiO_2	-48.4	11.6	2.8	1.85	S1
MXene/ZnO	-26.3	17.4	1.4	4	S2
MXene/$Ni_{0.5}Zn_{0.5}Fe_2O_4$	-42.5	13.5	3	6.5	S3
MXene/PVB/$Ba_3Co_2Fe_{24}O_{41}$	-46.3	5.8	1.6	2.8	S4
MXene/Ni-modified	-18.2	16.2	6.3	1.5	S5
MXene/Co_3O_4	-34.5	14	6.3	2.0	S6
MXene/FeCo	-17.86	-	8.8	1.6	S7
MXene/CoFe	-36.29	8.56	2.64	2.2	S8
MXene/TiO_2/MoS_2	~ -16	~ 9.8	2.6	2.5	S9
MXene/Fe_3O_4/PANI	-40.3	15.3	5.2	1.9	S10
MXene/Ni chain	-49.9	11.9	2.1	1.75	S11
MXene/carbonyl iron	-15.52	12.8	8.16	1	S12
MXene/Ni	**-50.5**	**5.5**	**5.28**	**3.5**	**this work**

Compared with other MXene-based composites (Table S1), the M/N absorbers prepared in this work showed distinct advantages due to its both excellent absorption performance and wide absorption band.

S1. Han, M.; Yin, X.; Wu, H.; Hou, Z.; Song, C.; Li, X.; Zhang, L.; Cheng, L., Ti_3C_2 MXenes with Modified Surface for High-Performance Electromagnetic Absorption and Shielding in the X-Band. *ACS Appl. Mater. Interfaces* **2016,** *8* (32), 21011-21019.

S2. Qian, Y.; Wei, H.; Dong, J.; Du, Y.; Fang, X.; Zheng, W.; Sun, Y.; Jiang, Z., Fabrication of Urchin-Like ZnO-MXene Nanocomposites for High-Performance

Electromagnetic Absorption. *Ceramics International* **2017,** *43* (14), 10757-10762.

S3. Li, Y.; Zhou, X.; Wang, J.; Deng, Q.; Li, M.; Du, S.; Han, Y.-H.; Lee, J.; Huang, Q., Facile Preparation of In-Situ Coated $Ti_3C_2T_x/Ni_{0.5}Zn_{0.5}Fe_2O_4$ Composites and Their Electromagnetic Performance. *RSC Adv.* **2017,** *7* (40), 24698-24708.

S4. Yang, H.; Dai, J.; Liu, X.; Lin, Y.; Wang, J.; Wang, L.; Wang, F., Layered PVB/$Ba_3Co_2Fe_{24}O_{41}/Ti_3C_2$ MXene Composite: Enhanced Electromagnetic Wave Absorption Properties with High Impedance Match in a Wide Frequency Range. *Materials Chemistry and Physics* **2017,** *200*, 179-186.

S5. Feng, W.; Luo, H.; Zeng, S.; Chen, C.; Deng, L.; Tan, Y.; Zhou, X.; Peng, S.; Zhang, H., Ni-Modified Ti_3C_2 MXene with Enhanced Microwave Absorbing Ability. *Materials Chemistry Frontiers* **2018,** *2* (12), 2320-2326.

S6. Deng, R.; Chen, B.; Li, H.; Zhang, K.; Zhang, T.; Yu, Y.; Song, L., MXene/Co_3O_4 Composite Material: Stable Synthesis and Its Enhanced Broadband Microwave Absorption. *Applied Surface Science* **2019,** *488*, 921-930.

S7. He, J.; Shan, D.; Yan, S.; Luo, H.; Cao, C.; Peng, Y., Magnetic FeCo Nanoparticles-Decorated Ti_3C_2 MXene with Enhanced Microwave Absorption Performance. *J. Magn. Magn. Mater.* **2019,** *492, 1656391-1656396*.

S8. Zhou, C.; Wang, X.; Luo, H.; Deng, L.; Wang, S.; Wei, S.; Zheng, Y.; Jia, Q.; Liu, J., Interfacial Design of Sandwich-Like CoFe@$Ti_3C_2T_x$ Composites as High Efficient Microwave Absorption Materials. *Applied Surface Science* **2019,** *494*, 540-550.

S9. Wang, H.; Ma, H., The Electromagnetic and Microwave Absorbing Properties of MoS_2 Modified $Ti_3C_2T_x$ Nanocomposites. *J. Mater. Sci. Mater. Electron.* **2019,** *30* (16), 15250-15256.

S10. Wang, Y.; Gao, X.; Zhang, L.; Wu, X.; Wang, Q.; Luo, C.; Wu, G., Synthesis of Ti_3C_2/Fe_3O_4/PANI Hierarchical Architecture Composite as an Efficient Wide-Band Electromagnetic Absorber. *Applied Surface Science* **2019,** *480*, 830-838.

S11. Liang, L.; Han, G.; Li, Y.; Zhao, B.; Zhou, B.; Feng, Y.; Ma, J.; Wang, Y.; Zhang, R.; Liu, C., Promising $Ti_3C_2T_x$ MXene/Ni Chain Hybrid with Excellent Electromagnetic Wave Absorption and Shielding Capacity. *ACS Appl. Mater. Interfaces* **2019,** *11* (28), 25399-25409.

S12. Yan, S.; Cao, C.; He, J.; He, L.; Qu, Z., Investigation on the Electromagnetic and Broadband Microwave Absorption Properties of Ti_3C_2 Mxene/flaky Carbonyl Iron Composites. *J. Mater. Sci. Mater. Electron*. **2019**, 30 (7), 6537-6543.

S13. Deng, R.; Chen, B.; Li, H.; Zhang, K.; Zhang, T.; Yu, Y.; Song, L., MXene/Co_3O_4 Composite Material: Stable Synthesis and Its Enhanced Broadband Microwave Absorption. *Applied Surface Science* **2019**, 488, 921-930.

S14. Zhang, X.; Wang, H.; Hu, R.; Huang, C.; Zhong, W.; Pan, L.; Feng, Y.; Qiu, T.; Zhang, C.; Yang, J., Novel Solvothermal Preparation and Enhanced Microwave Absorption Properties of $Ti_3C_2T_x$ MXene Modified by In-Situ Coated Fe_3O_4 Nanoparticles. *Applied Surface Science* **2019**, 484, 383-391.

S15. Liu, P.; Yao, Z.; Ng, V. M. H.; Zhou, J.; Kong, L. B., Novel Multilayer-Like Structure of $Ti_3C_2T_x$/CNZF Composites for Low-Frequency Electromagnetic Absorption. *Mater. Lett.* **2019**, 248, 214-217.

The basic principle of geometric phase analysis is as follows:

For a perfect crystal, a HRTEM can be described as a Fourier series:

$$I(r) = \sum_g H_g e^{2\pi i g \cdot r} \quad (1)$$

Where I(r) is the image intensity at the position r, g is the periodicities of the Bragg reflections, the Fourier coefficients H_g can be described as:

$$H(g) = A_g e^{ip_g} \quad (2)$$

Where A_g is the amplitude of the set of sinusoidal lattice fringes g, P_g is the lateral position of the fringes in the original image.

In real image conditions, the Fourier coefficient H_g has conjugate symmetry. Image strength can be expressed as the following real number function:

$$I(r) = A_0 + \sum_{g>0} 2A_g \cos(2\pi g \cdot r + p_g) \quad (3)$$

When processing the actually captured high-resolution image, the lattice image is subjected to fast Fourier transform processing to obtain an inverted space bitmap. A specific $\pm$g direction lattice is selected by a mask to obtain a specific direction stripe information, and then an inverse Fourier transform is performed to obtain a lattice fringe $B_g(r)$ in the specific direction:

$$B_g(r) = 2A_g \cos(2\pi g \cdot r + p_g) \quad (4)$$

In order to describe the lattice changes caused by distortion and defects in the material, the amplitude and phase of the lattice fringes should be expressed by the functions $A_g(r)$ and $P_g(r)$ for the position π, which should be written as:

$$B_g(r) = 2A_g(r) \cos(2\pi g \cdot r + p_g(r)) \quad (5)$$

The basic principle of electron holography analysis is as follows:

According to the simplified Poisson's equation about the electrostatic field theory, the charge density can be calculated from

$$\rho(\chi) = -\varepsilon_\gamma \varepsilon_0 \frac{\partial^2 v(\chi)}{\partial \chi^2} \quad (6)$$

where $\rho(\chi)$ is the charge density, χ is the distance, ε_γ and ε_o are the relative dielectric constant in sample and the dielectric constant in vacuum, respectively.